

Proposal for Detecting Nodal-Line Semimetal Surface States with Resonant Spin-Flipped Reflection


Wei Chen,^{1,2,*} Kun Luo,² Lin Li,^{3,4} and Oded Zilberberg¹

¹*Institute for Theoretical Physics, ETH Zurich, 8093 Zürich, Switzerland*

²*College of Science, Nanjing University of Aeronautics and Astronautics, Nanjing 210016, China*

³*College of Physics and Electronic Engineering, and Center for Computational Sciences, Sichuan Normal University, Chengdu 610068, China*

⁴*Shenzhen Institute for Quantum Science and Engineering and Department of Physics, Southern University of Science and Technology, Shenzhen 518055, China*

 (Received 31 January 2018; revised manuscript received 23 May 2018; published 17 October 2018)

Topological nodal-line semimetals are predicted to exhibit unique drumheadlike surface states (DSSs). Yet, direct detection of such states remains a challenge. Here, we propose spin-resolved transport in a junction between a normal metal and a spin-orbit coupled nodal-line semimetal as the mechanism for their detection. Specifically, we find that in such an interface the DSSs induce resonant spin-flipped reflection. This effect can be probed by both vertical spin transport and lateral charge transport between antiparallel magnetic terminals. In the tunneling limit of the junction, both spin and charge conductances exhibit a resonant peak around zero energy, providing unique evidence of the DSSs. This signature is robust to both dispersive DSSs and interface disorder. Based on numerical calculations, we show that the scheme can be implemented in the topological semimetal HgCr_2Se_4 .

DOI: [10.1103/PhysRevLett.121.166802](https://doi.org/10.1103/PhysRevLett.121.166802)

The discovery of topological materials has evinced one of the main recent advances in condensed matter physics [1–3]. Depending on whether the bulk states are gapped or gapless, topological materials can be largely divided into topological insulator phases [1,2] and topological semimetal phases [4]. In both categories, the material's bulk bands are characterized by topological invariants, which additionally result in gapless surface states according to a bulk-boundary correspondence [5]. Therefore, detection of topological surface states is key for the identification of topological materials. For insulating phases, the edge or surface states are energetically well separated from the bulk ones, and can be readily identified by transport measurement [6,7], scanning tunneling microscopy [8,9], or angle-resolved photoemission spectroscopy (ARPES) [10]. Topological semimetals are more subtle, because the Fermi level crosses both the bulk and the surface states. Nevertheless, extensive progress has been achieved on the observation of exotic Fermi arc states in Weyl and Dirac semimetals [11–13] by ARPES [14] and transport measurements [15].

Recently, another kind of topological semimetal, a nodal-line semimetal (NLS), has attracted increasing research interests [16–33]. These 3D materials are characterized by band crossings along closed loops, with each loop carrying a π Berry flux [16]. A direct result of the NLS band topology is the existence of drumheadlike surface states (DSSs) nestled inside the projection of the nodal loops onto the 2D surface Brillouin zone [20]. There are a

variety of candidates for a NLS [17–29], and their experimental characterization has seen recent progress using ARPES [29,34–37] and quantum oscillation [38–41] measurements. However, direct evidence of novel DSSs, the hallmark of a NLS, is still missing: in the ARPES experiments, the surface states are veiled in the bulk bands, which can only be identified via a comparison with the results of a first-principles' calculation; the experiments on quantum oscillations only focus on bulk states, so that no information on the surface states can be extracted.

In this Letter, we propose two types of transport experiments for the detection of the DSSs. These experiments rely on the spin-resolved scattering in a junction between a normal metal and a NLS, see Fig. 1(a). The DSSs induce a resonant spin-flipped reflection (RSFR) for spin-polarized (along the z axis) electrons incident from the normal metal. This effect manifests in a nearly pure spin current flowing perpendicular to the junction [Fig. 2(a)], or in a lateral charge transport between two antiparallel magnetic terminals [Fig. 2(d)]. In the tunneling limit, both setups show a resonant peak in their spin or charge conductance around the energy level of the nodal loop, that can serve as a direct evidence of the DSSs. We analytically detail our predictions in a minimal NLS model and numerically demonstrate these signatures for a real material HgCr_2Se_4 [42].

We consider spin-polarized electrons incident in the z direction, see Fig. 1(a). We assume that the incident electron spin is polarized in the z direction and is injected into the metal ($z < 0$) by a ferromagnetic lead. In the $z > 0$

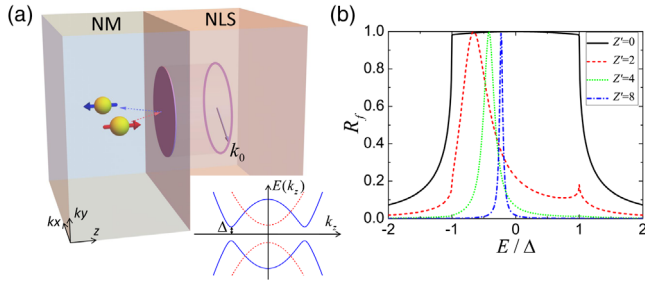


FIG. 1. (a) Schematic illustration of a junction between a normal metal and a nodal line semimetal (NLS). The drumheadlike surface states at the boundary are encircled by the projection of the bulk nodal loop onto the surface Brillouin zone. Whenever an incident electron from the metal is reflected, its spin is flipped when the transverse momentum lies inside the drumhead. The inset shows the k_z -dependent energy bands of effective 1D channels in the z direction when the transverse momentum \mathbf{k}_{\parallel} lies inside (blue solid lines) and outside (red dashed lines) the drumhead. (b) Probability of spin-flipped reflection at the boundary between the materials as a function of energy with the following parameters: $\theta = \pi/6$, $k_F = 1.1k_0 = 1.54$, $C = B = 1$, $\lambda = 0.01$, cf. Eq. (2).

region, we use a minimal continuous model to describe the nodal-line semimetal as

$$H_{\text{SM}}(\mathbf{k}) = \lambda k_z \sigma_x + B(k_0^2 - |\mathbf{k}|^2) \sigma_z, \quad (1)$$

where $|\mathbf{k}|^2 = k_x^2 + k_y^2 + k_z^2$ is the total momentum squared and the Pauli matrices $\sigma_{x,z}$ operate in the spin space. The Hamiltonian Eq. (1) has eigenvalues $E_{\pm} = \pm \sqrt{\lambda^2 k_z^2 + B^2(k_0^2 - |\mathbf{k}|^2)^2}$ and corresponding eigenstates $|u_{\pm}(\mathbf{k})\rangle$. The resulting two bands are degenerate at $k_x^2 + k_y^2 = k_0^2$ and $k_z = 0$, thus defining a nodal loop in momentum space, see Fig. 1(a). Considering the transverse wave vector $\mathbf{k}_{\parallel} = (k_x, k_y)$ as a parameter, the Hamiltonian Eq. (1) describes an effective 1D system in the z direction. Whenever \mathbf{k}_{\parallel} lies inside the nodal loop, that is $|\mathbf{k}_{\parallel}| < k_0$, the effective 1D system is insulating with an energy gap $\Delta(\mathbf{k}_{\parallel}) = \lambda k'_0$ opening around $k_z = k'_0 = \sqrt{k_0^2 - |\mathbf{k}_{\parallel}|^2}$, see inset of Fig. 1(a). The gap varies with \mathbf{k}_{\parallel} , and reaches its maximum $\Delta_0 = \lambda k_0$ at $\mathbf{k}_{\parallel} = 0$. Interestingly, the effective 1D model has a nontrivial band topology that is characterized by the Berry phase $\gamma_B = \pi$, with $\gamma_B = i \int_{-\infty}^{\infty} dk_z \langle u_{-}(\mathbf{k}) | \partial_{k_z} | u_{-}(\mathbf{k}) \rangle$ [3,26]. In the presence of chiral symmetry, such nontrivial topological winding implies the appearance of a zero-energy end state at an open boundary [45,46]. As \mathbf{k}_{\parallel} varies inside the nodal loop, these topological end states appear and form the DSSs, which are encircled by the projection of the nodal loop onto the surface Brillouin zone, see Fig. 1(a). When the transverse

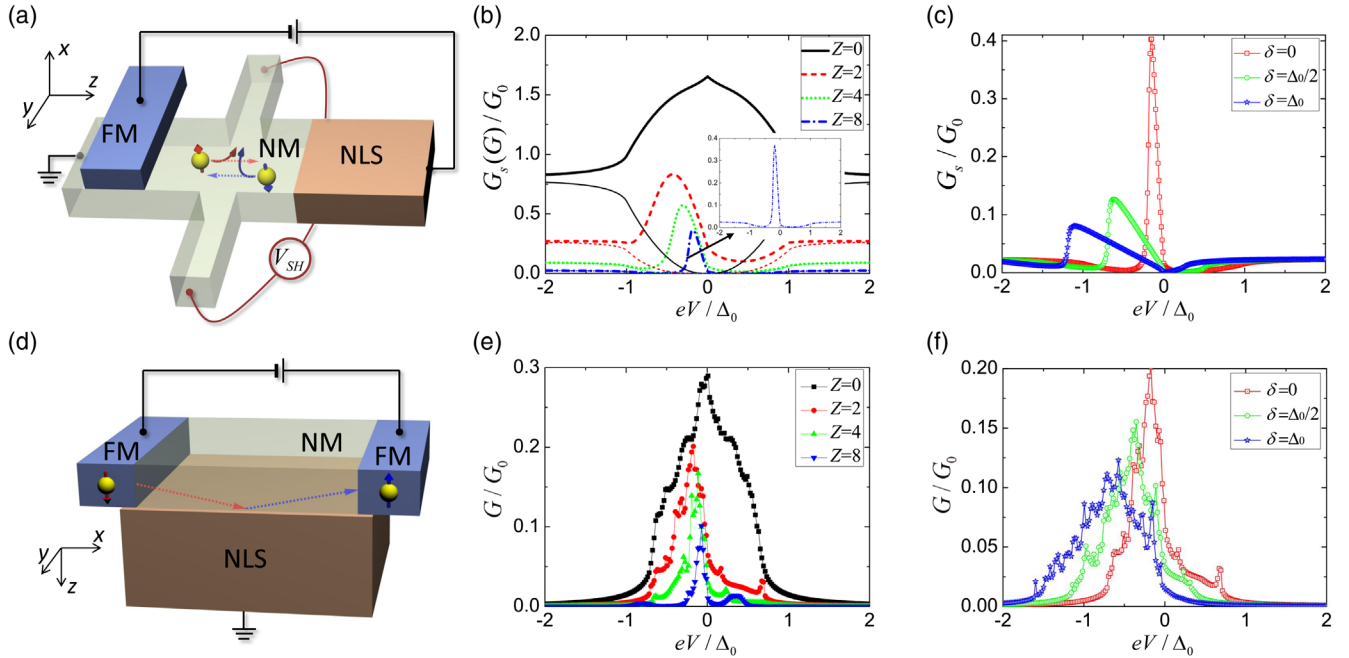


FIG. 2. (a) Setup for spin transport DSSs detection. A normal metal with weak spin-orbit coupling, such as Al, Au, is fabricated into a Hall cross. Spin-up electrons are injected from a ferromagnetic metal (FM). The inverse spin Hall effect in the normal metal results in a transverse drift of electrons, yielding a transverse voltage drop V_{SH} between two Hall probes [43,44]. (b) Spin (thick lines) and charge (thin lines) conductance for different interface barrier heights, cf. Eq. (3). Inset: Zoom of the sharp peak with $Z = 8$. (c) Effect of finite dispersion of the DSSs on spin conductance with $Z = 10$. (d) Setup for charge transport DSSs detection. The polarizations of the FM leads are taken to be antiparallel and transport through the device is possible only due to spin-flipping processes at the metal-NLS boundary. (e) Charge conductance for different interface barrier heights. (f) Effect of finite dispersion of the DSSs on charge conductance with $Z = 2$. All other parameters are the same as those taken in Fig. 1.

wave vector \mathbf{k}_{\parallel} lies outside the nodal loop, the effective 1D system becomes a trivial insulator with an energy gap around $k_z = 0$ [inset of Fig. 1(a)], and no surface states show up at an open boundary.

In the $z < 0$ region, lies the spin-degenerate normal metal, described by the Hamiltonian $H_{\text{NM}} = C|\mathbf{k}|^2 - \mu_0$, where C is a mass dependent parameter and μ_0 is the chemical potential corresponding to the Fermi wave vector $|\mathbf{k}_F| = \sqrt{\mu_0/C}$. The interface scattering is considered using a Dirac-type barrier $U\delta(z)$. The scattering of the incident electron from the normal metal onto the NLS is solved by substituting $k_z = -i\partial_z$ and keeping \mathbf{k}_{\parallel} a good quantum number [47]. Importantly, we obtain that incident spin-up electrons with $|\mathbf{k}_{\parallel}| < k_0$ engender a spin-flipped reflection amplitude [47]

$$r_f = -\frac{4}{(\eta + 1/\eta + iZ')^2 \Upsilon_1 + (\eta - 1/\eta + iZ')^2 / \Upsilon_1}, \quad (2)$$

where $\eta = \sqrt{v_{\text{NM}}/v_{\text{SM}}}$ is the square root of the ratio of perpendicular velocities in the normal metal and NLS, with $v_{\text{NM}} = 2C|\mathbf{k}_F| \cos \theta$ and $v_{\text{SM}} = 2Bk'_0$, respectively, θ is the electron's incident angle (relative to the z axis), $Z' = 2U/\sqrt{v_{\text{NM}}v_{\text{SM}}}$ is a dimensionless interface barrier height, and $\Upsilon_1 = [E + B(k_1^2 - k_0^2)]/(k_1\lambda)$ with $k_1 = \sqrt{k_0^2 - (\lambda^2 - \sqrt{4E^2B^2 + \lambda^4 - 4\lambda^2B^2k_0^2})/(2B^2)}$.

The obtained spin-flipped reflection probability, $R_f = |r_f|^2$, exhibits a sharp resonant peak around zero energy in the tunneling limit ($Z' \gg 1$), see Fig. 1(b) [51]. This result can be understood by rewriting Eq. (2) in the tunneling limit as a summation over Feynman paths constructed by multiple reflection between the barrier and the NLS surface [47,52]. It turns out that the condition of RSFR is identical to the Bohr-Sommerfeld quantization condition for a surface bound state, which indicates that the RSFR is directly induced by the topological surface state.

Moreover, this scenario can also be understood by a tunneling Hamiltonian description. In the tunneling limit, for each 1D channel inside the nodal loop ($|\mathbf{k}_{\parallel}| < k_0$), we can use a tunneling Hamiltonian to describe the coupling between the DSSs and the normal metal as $H_T = \sum_{k_z} V_k (c_{k\uparrow}^\dagger + ic_{k\downarrow}^\dagger) \gamma_{k_{\parallel}} + \text{H.c.}$, where $\gamma_{k_{\parallel}} = \int dz (f_{k_{\parallel}}^*(z)/\sqrt{2}) [\psi_{\uparrow}(z) - i\psi_{\downarrow}(z)]$ is the Fermi operator for the DSSs exhibiting some spatial distribution $f_{k_{\parallel}}(z)$, $c_{k\uparrow,\downarrow}$ are annihilation operators of electron in the normal metal, and V_k is the coupling strength [47]. The DSSs are spin-polarized along the y direction [47], thus resulting in an equal coupling strength to both spin states in the normal metal. Such a tunneling Hamiltonian has the same form as that of a resonant tunneling through a single-level system [53], when we regard the two spin states in the normal metal as two spinless leads and the surface state in each

\mathbf{k}_{\parallel} channel as the single level. A direct calculation leads to a result of RSFR with a Lorentzian form, i.e., $R_f(E) = \Gamma^2/(E^2 + \Gamma^2)$ (Γ is level-width function) [47], which is consistent with the result in Fig. 1(b).

We propose two experimental schemes to probe the RSFR: (i) vertical spin transport in the setup in Fig. 2(a), and (ii) lateral charge transport in the setup in Fig. 2(d). For scheme (i), spin-polarized electrons are injected from a ferromagnetic lead, and then reflected with spin flipping at the junction. The resulting nearly pure spin current can be measured as a spin Hall voltage V_{SH} [54] in the inverse spin Hall effect [43,44], see Fig. 2(a). For scheme (ii), charge current flows between two antiparallel magnetic terminals, which cannot happen without the spin-flipped reflection. The RSFR can be well characterized in both setups by a resonant peak in the spin or charge conductance.

The spin current in setup (i) is defined as $I_s = I_{\uparrow} - I_{\downarrow}$, where I_{σ} with $\sigma = \uparrow, \downarrow$ are spin-polarized currents flowing in the z direction. In order to generate the spin Hall voltage, the spin is polarized along the x direction, see Fig. 2(a). In the RSFR regime, incident and reflected electrons have opposite spin polarizations as well as opposite velocities. Consequently, the RSFR enhances the spin current, while the charge current $I = I_{\uparrow} + I_{\downarrow}$ is strongly suppressed. This results in a nearly pure spin current flowing in the normal metal. To reveal the energy dependence of the spin transport, we calculate the differential spin conductance $G_s(eV) = \partial I_s / \partial V$ [55] using

$$G_s(E) = G_0 \int_0^{\pi/2} d\theta \sin 2\theta [1 + R_f(\theta, E) - R_c(\theta, E)], \quad (3)$$

where $G_0 = (\mathcal{A}k_F^2/4\pi)(e^2/h)$ is the single-spin conductance of the uniform normal metal with a cross section area \mathcal{A} , and $R_c = |r_c|^2$ is the probability of spin-conserved reflection. The spin conductance G_s as a function of the bias voltage eV for different barrier strengths $Z = U/\sqrt{C|\mathbf{k}_F|Bk_0}$ is plotted in Fig. 2(b). In the transparent case ($Z = 0$), G_s exhibits a heightened ridge in the region $eV \in (-\Delta_0, \Delta_0)$, corresponding to strong spin-flipped reflection below the gap Δ_0 [Fig. 1(b)]. As Z increases, a narrower peak forms and moves towards zero energy, as expected for RSFR. At the same time, the height of the peak reduces because the RSFR peaks become sharper in all transport channels [Fig. 1(b)], and the resonant energies do not match one another. Note that although the reduced spin conductance becomes small in the tunneling limit, the absolute value of G_s around the resonant peak is still quite large. Concurrently, the charge conductance $G = \partial I / \partial V$ becomes much smaller than G_s within the gap, indicating a high-purity spin current, see Fig. 2(b). Outside the gap, G_s and G tend to be equal, and transmission through the barrier (rather than RSFR) dominates the transport.

In real materials, chiral symmetry is usually broken on the open surface, and the DSSs are commonly dispersive.

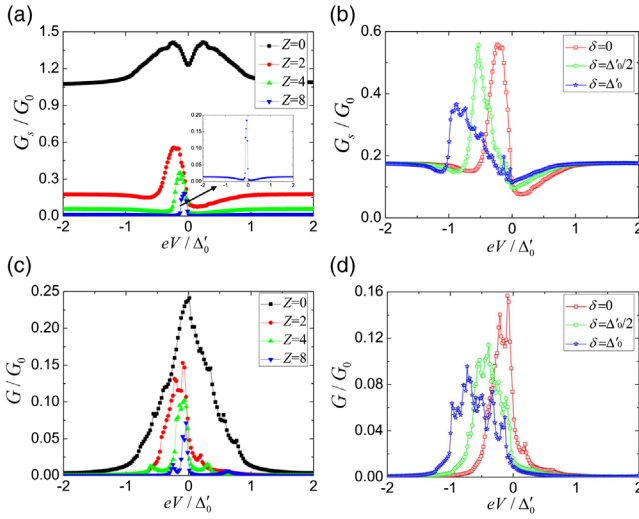


FIG. 3. Numerical results for HgCr_2Se_4 . Spin conductance of vertical spin transport for different (a) interface barriers, and (b) dispersions of DSSs (with $Z = 2$). Inset in (a): Zoom of the peak structure with $Z = 8$. Charge conductance of lateral charge transport for different (c) interface barriers, and (d) dispersions of DSSs (with $Z = 2$). All the parameters are the same as those in Fig. 1, except that $D = 0.01/k_0^2$.

To model this effect, we add a spin independent term $\varepsilon(\mathbf{k}_{\parallel}) = A_1(|\mathbf{k}_{\parallel}|^2 - k_0^2)$ to Eq. (1). This introduces a bandwidth $\delta = A_1 k_0^2$ to the DSSs. Such a \mathbf{k}_{\parallel} -dependent potential leads to further separation of RSFR levels in different channels. As a result, the peak of G_s is broadened and also shifted, as shown in Fig. 2(c). In the tunneling limit, the width of the resonant peak is approximately equal to the width of the surface band δ , so that the bandwidth of the DSSs can be directly inferred from the width of the resonant peak in G_s [47], see also Figs. 2(f), 3(b), and 3(d).

The charge current in setup (ii) [Fig. 2(d)] flows in the normal metal in the x direction, parallel to the interface of the junction. The normal metal is sandwiched by two antiparallel ferromagnetic terminals. Without spin-flipped reflection at the junction, electrons injected from one terminal cannot enter the other. Therefore, setup (ii) can be used to detect the RSFR. The conductance G is calculated numerically (using KWANT [48]) based on a lattice version of our model [47], see Fig. 2(e). The conductance is normalized by G_0 , the single-spin conductance in the x direction through the normal metal. In the transparent limit of the junction ($Z = 0$), electrons transport in the energy window $eV \in (-\Delta_0, \Delta_0)$, corresponding to the energy scale of spin-flipped reflection. As Z increases, G exhibits a sharp peak around zero energy, which signals the RSFR. In the setup in Fig. 2(d), multiple scattering occurs at all the surfaces of the normal metal, so that the conductance shows fluctuation. The effect of finite dispersion of the DSSs is also investigated, and the results are shown in Fig. 2(f). It shifts and spreads the resonant

peak, similar to the results reported for the spin transport in scheme (i), cf. Fig. 2(c).

In realistic setups, there would be several additional imperfections that should be taken into account, such as interface imperfections and nonpure spin injection [56]. In experiments, interface imperfections commonly exist, such that the clean tunneling limit is difficult to obtain. For both transport schemes, we numerically investigate this effect by introducing interface disorder (see Fig. S.2 in the Supplemental Material [47]). One can see that apart from some broadening of the general features, the resonant peak in the spin and charge conductances is robust to strong disorder with the strength close to the interface barrier, reflecting the robustness of topological DSSs. Similarly, spin-polarization averaging leads to an overall reduction prefactor that does not qualitatively change the overall transport signatures [47].

Our analysis has, thus far, relied on a minimal NLS model [Eq. (1)]. For experimental realizations, we consider the topological semimetal HgCr_2Se_4 [42] as a promising candidate. In the $|J, M_J\rangle$ basis $|\frac{3}{2}, \frac{3}{2}\rangle = (1/\sqrt{2})|(X + iY)\uparrow\rangle$ and $|S\downarrow\rangle$, an effective two-band model for HgCr_2Se_4 can be written as

$$H_{\text{HCS}}(\mathbf{k}) = \begin{pmatrix} B(k_0^2 - |\mathbf{k}|^2) & Dk_z k_{\pm}^2 \\ Dk_z k_{\pm}^2 & -B(k_0^2 - |\mathbf{k}|^2) \end{pmatrix}, \quad (4)$$

with $k_{\pm} = k_x \pm ik_y$. The eigenenergies of this model are $E'_{\pm} = \pm\sqrt{B^2(k_0^2 - |\mathbf{k}|^2)^2 + D^2 k_z^2 |\mathbf{k}_{\parallel}|^4}$. Therefore, the gap closes along exactly the same nodal line as that of the minimal model Eq. (1). For each \mathbf{k}_{\parallel} channel, the effective gap is $\Delta'(\mathbf{k}_{\parallel}) = Dk_0' |\mathbf{k}_{\parallel}|^2$, and its maximum is $\Delta'_0 = 2Dk_0^3/(3\sqrt{3})$ when $|\mathbf{k}_{\parallel}| = \sqrt{2/3}k_0$. Additionally, the model Eq. (4) exhibits two Weyl nodes in the z axis at $k_z = \pm k_0$. The Weyl nodes only introduce a single gapless 1D channel, and the corresponding Fermi-arc surface states do not appear at an open boundary in the z direction, so that the DSSs remain the dominating transport effect at a metal-NLS junction in Fig. 1(a).

We numerically calculate the spin and charge conductances in schemes (i) and (ii) [Figs. 2(a) and 2(d)] for the lattice version of Eq. (4) [47]. All the results agree well with those of the minimal model. G_s and G for different barrier heights are shown in Figs. 3(a) and 3(c). For a transparent junction, G_s is heightened and G has a peak spreading in the energy window $eV \in (-\Delta'_0, \Delta'_0)$, which is generated by the spin-flipped reflection. As Z increases, a resonant peak shows up, indicating the DSSs induced RSFR. The effect of dispersive DSSs is shown in Figs. 3(b) and 3(d) and leads to widening of the RSFR peak. The resonant peak is robust against interface disorder and nonpure spin injection [47].

It is worthwhile to compare the DSSs induced RSFR with other spin relaxation processes. Most spin relaxation

mechanisms can only lead to weak dissipation of spin signatures [57], strongly different from the RSFR-induced enhancement of the spin signature. Consider, for example, spin-flipped scattering induced by magnetic impurities at the interface of the junction: in order to obtain a comparable resonance strength, a high density of impurities with the same energy level is required. Similarly, the electrons will have a very small rate of colliding with bulk impurities due to the vanishing density of states in the bulk of the NLS.

To conclude, we have shown that resonant spin-flipped reflection can serve as unambiguous evidence of the drumheadlike surface states in the spin-orbit coupled nodal-line semimetal. Recent experimental progress on spin-resolved transport in HgCr_2Se_4 [58] paves the way to the realization of our proposal. Our analysis can be extended to other types of nodal-line semimetals, i.e., both to additional materials but also engineered systems such as photonic nodal-line systems.

We thank Chen Fang, Gang Xu, Wei-Yin Deng, Di Wu, Zhong Wang, J.L. Lado, and Michael S. Ferguson for helpful discussions and Hu Zhao for assistance on the figures. This work was supported by the National Natural Science Foundation of China under Grants No. 11504171 (W.C.), No. 11604138 (L.L.) and by the Natural Science Foundation of Jiangsu Province in China under Grant No. BK20150734. W.C. acknowledges the support from the Swiss Government Excellence Scholarship under the program of China Scholarships Council (No. 201600160112). O.Z. acknowledges financial support from the Swiss National Science Foundation.

*pchenweis@gmail.com

- [1] M. Z. Hasan and C. L. Kane, Colloquium: Topological insulators, *Rev. Mod. Phys.* **82**, 3045 (2010).
- [2] X.-L. Qi and S.-C. Zhang, Topological insulators and superconductors, *Rev. Mod. Phys.* **83**, 1057 (2011).
- [3] C.-K. Chiu, J. C. Y. Teo, A. P. Schnyder, and S. Ryu, Classification of topological quantum matter with symmetries, *Rev. Mod. Phys.* **88**, 035005 (2016).
- [4] H. Weng, X. Dai, and Z. Fang, Topological semimetals predicted from first-principles calculations, *J. Phys. Condens. Matter* **28**, 303001 (2016).
- [5] B. I. Halperin, Quantized hall conductance, current-carrying edge states, and the existence of extended states in a two-dimensional disordered potential, *Phys. Rev. B* **25**, 2185 (1982).
- [6] M. König, S. Wiedmann, C. Brüne, A. Roth, H. Buhmann, L. W. Molenkamp, X.-L. Qi, and S.-C. Zhang, Quantum spin hall insulator state in HgTe quantum wells, *Science* **318**, 766 (2007).
- [7] A. Roth, C. Brüne, H. Buhmann, L. W. Molenkamp, J. Maciejko, X.-L. Qi, and S.-C. Zhang, Nonlocal transport in the quantum spin hall state, *Science* **325**, 294 (2009).
- [8] P. Roushan, J. Seo, C. V. Parker, Y. S. Hor, D. Hsieh, D. Qian, A. Richardella, M. Z. Hasan, R. J. Cava, and A. Yazdani, Topological surface states protected from backscattering by chiral spin texture, *Nature (London)* **460**, 1106 (2009).
- [9] T. Zhang *et al.*, Experimental Demonstration of Topological Surface States Protected by Time-Reversal Symmetry, *Phys. Rev. Lett.* **103**, 266803 (2009).
- [10] D. Hsieh, D. Qian, L. Wray, Y. Xia, Y. S. Hor, R. J. Cava, and M. Z. Hasan, A topological Dirac insulator in a quantum spin hall phase, *Nature (London)* **452**, 970 (2008).
- [11] S. Murakami, Phase transition between the quantum spin hall and insulator phases in 3D: Emergence of a topological gapless phase, *New J. Phys.* **9**, 356 (2007).
- [12] X. Wan, A. M. Turner, A. Vishwanath, and S. Y. Savrasov, Topological semimetal and fermi-arc surface states in the electronic structure of pyrochlore iridates, *Phys. Rev. B* **83**, 205101 (2011).
- [13] H. Weng, C. Fang, Z. Fang, B. A. Bernevig, and X. Dai, Weyl Semimetal Phase in Noncentrosymmetric Transition-Metal Monophosphides, *Phys. Rev. X* **5**, 011029 (2015).
- [14] Z. K. Liu *et al.*, Discovery of a three-dimensional topological Dirac semimetal, Na_3Bi , *Science* **343**, 864 (2014).
- [15] P. J. W. Moll, N. L. Nair, T. Helm, A. C. Potter, I. Kimchi, A. Vishwanath, and J. G. Analytis, Transport evidence for fermi-arc-mediated chirality transfer in the Dirac semimetal Cd_3As_2 , *Nature (London)* **535**, 266 (2016).
- [16] A. A. Burkov, M. D. Hook, and L. Balents, Topological nodal semimetals, *Phys. Rev. B* **84**, 235126 (2011).
- [17] Y. Kim, B. J. Wieder, C. L. Kane, and A. M. Rappe, Dirac Line Nodes in Inversion-Symmetric Crystals, *Phys. Rev. Lett.* **115**, 036806 (2015).
- [18] R. Yu, H. Weng, Z. Fang, X. Dai, and X. Hu, Topological Node-Line Semimetal and Dirac Semimetal State in Antiperovskite Cu_3PdN , *Phys. Rev. Lett.* **115**, 036807 (2015).
- [19] T. T. Heikkilä, N. B. Kopnin, and G. E. Volovik, Flat bands in topological media, *JETP Lett.* **94**, 233 (2011).
- [20] H. Weng, Y. Liang, Q. Xu, R. Yu, Z. Fang, X. Dai, and Y. Kawazoe, Topological node-line semimetal in three-dimensional graphene networks, *Phys. Rev. B* **92**, 045108 (2015).
- [21] Y. Chen, Y. Xie, S. A. Yang, H. Pan, F. Zhang, M. L. Cohen, and S. Zhang, Nanostructured carbon allotropes with Weyl-like loops and points, *Nano Lett.* **15**, 6974 (2015), PMID: 26426355.
- [22] M. Zeng, C. Fang, G. Chang, Y.-A. Chen, T. Hsieh, A. Bansil, H. Lin, and L. Fu, Topological semimetals and topological insulators in rare earth mononictides, [arXiv: 1504.03492](https://arxiv.org/abs/1504.03492).
- [23] C. Fang, Y. Chen, H.-Y. Kee, and L. Fu, Topological nodal line semimetals with and without spin-orbital coupling, *Phys. Rev. B* **92**, 081201 (2015).
- [24] A. Yamakage, Y. Yamakawa, Y. Tanaka, and Y. Okamoto, Line-node Dirac semimetal and topological insulating phase in noncentrosymmetric pnictides CaAg_x ($x = p, \text{As}$), *J. Phys. Soc. Jpn.* **85**, 013708 (2016).
- [25] L. S. Xie, L. M. Schoop, E. M. Seibel, Q. D. Gibson, W. Xie, and R. J. Cava, A new form of Ca_3P_2 with a ring of Dirac nodes, *APL Mater.* **3**, 083602 (2015).
- [26] Y.-H. Chan, C.-K. Chiu, M. Y. Chou, and A. P. Schnyder, Ca_3P_2 and other topological semimetals with line nodes and drumhead surface states, *Phys. Rev. B* **93**, 205132 (2016).

- [27] J. Zhao, R. Yu, H. Weng, and Z. Fang, Topological node-line semimetal in compressed black phosphorus, *Phys. Rev. B* **94**, 195104 (2016).
- [28] G. Bian *et al.*, Drumhead surface states and topological nodal-line fermions in TiTaSe_2 , *Phys. Rev. B* **93**, 121113 (2016).
- [29] G. Bian *et al.*, Topological nodal-line fermions in spin-orbit metal PbTaSe_2 , *Nat. Commun.* **7**, 10556 (2016).
- [30] T. Bzdušek, Q. Wu, A. Rüegg, M. Sgrist, and A. A. Soluyanov, Nodal-chain metals, *Nature (London)* **538**, 75 (2016).
- [31] W. Chen, H.-Z. Lu, and J.-M. Hou, Topological semimetals with a double-helix nodal link, *Phys. Rev. B* **96**, 041102 (2017).
- [32] Z. Yan, R. Bi, H. Shen, L. Lu, S.-C. Zhang, and Z. Wang, Nodal-link semimetals, *Phys. Rev. B* **96**, 041103 (2017).
- [33] M. Ezawa, Topological semimetals carrying arbitrary hopf numbers: Fermi surface topologies of a hopf link, solomon's knot, trefoil knot, and other linked nodal varieties, *Phys. Rev. B* **96**, 041202 (2017).
- [34] L. M. Schoop, M. N. Ali, C. Straßer, A. Topp, A. Varykhalov, D. Marchenko, V. Duppel, S. S. P. Parkin, B. V. Lotsch, and C. R. Ast, Dirac cone protected by non-symmorphic symmetry and three-dimensional Dirac line node in ZrSiS , *Nat. Commun.* **7**, 11696 (2016).
- [35] M. Neupane *et al.*, Observation of topological nodal fermion semimetal phase in ZrSiS , *Phys. Rev. B* **93**, 201104 (2016).
- [36] A. Topp, J. M. Lippmann, A. Varykhalov, V. Duppel, B. V. Lotsch, C. R. Ast, and L. M. Schoop, Non-symmorphic band degeneracy at the fermi level in ZrSiTe , *New J. Phys.* **18**, 125014 (2016).
- [37] D. Takane, Z. Wang, S. Souma, K. Nakayama, C. X. Trang, T. Sato, T. Takahashi, and Y. Ando, Dirac-node arc in the topological line-node semimetal HfSiS , *Phys. Rev. B* **94**, 121108 (2016).
- [38] J. Hu *et al.*, Evidence of topological nodal-line fermions in ZrSiSe and ZrSiTe , *Phys. Rev. Lett.* **117**, 016602 (2016).
- [39] J. Hu, Y. L. Zhu, D. Graf, Z. J. Tang, J. Y. Liu, and Z. Q. Mao, Quantum oscillation studies of the topological semimetal candidate ZrGem ($m = \text{S, Se, Te}$), *Phys. Rev. B* **95**, 205134 (2017).
- [40] N. Kumar, K. Manna, Y. Qi, S.-C. Wu, L. Wang, B. Yan, C. Felser, and C. Shekhar, Unusual magnetotransport from si-square nets in topological semimetal HfSiS , *Phys. Rev. B* **95**, 121109 (2017).
- [41] H. Pan *et al.*, Three-Dimensional Anisotropic Magnetoresistance in the Dirac Node-Line Material ZrSiSe , [arXiv:1708.02779](https://arxiv.org/abs/1708.02779).
- [42] G. Xu, H. Weng, Z. Wang, X. Dai, and Z. Fang, Chern Semimetal and the Quantized Anomalous Hall Effect in HgCr_2Se_4 , *Phys. Rev. Lett.* **107**, 186806 (2011).
- [43] S. O. Valenzuela and M. Tinkham, Direct electronic measurement of the spin hall effect, *Nature (London)* **442**, 176 (2006).
- [44] E. Saitoh, M. Ueda, H. Miyajima, and G. Tatara, Conversion of spin current into charge current at room temperature: Inverse spin-hall effect, *Appl. Phys. Lett.* **88**, 182509 (2006).
- [45] S. Ryu and Y. Hatsugai, Topological Origin of Zero-Energy Edge States in Particle-Hole Symmetric Systems, *Phys. Rev. Lett.* **89**, 077002 (2002).
- [46] M. Hirayama, R. Okugawa, T. Miyake, and S. Murakami, Topological Dirac nodal lines and surface charges in fcc alkaline earth metals, *Nat. Commun.* **8**, 14022 (2017).
- [47] See Supplemental Material at <http://link.aps.org/supplemental/10.1103/PhysRevLett.121.166802> for the effective continuous model and scattering approach, Feynman path explanation, tunneling Hamiltonian description, effect of surface dispersion, lattice model and numerical simulation, and effects of interface disorder and imperfect spin injection, which includes Refs. [48,49,50].
- [48] C. W. Groth, M. Wimmer, A. R. Akhmerov, and X. Waintal, KWANT: A software package for quantum transport, *New J. Phys.* **16**, 063065 (2014).
- [49] D. J. BenDaniel and C. B. Duke, Space-charge effects on electron tunneling, *Phys. Rev.* **152**, 683 (1966).
- [50] U. Zülicke and C. Schroll, Interface Conductance of Ballistic Ferromagnetic-Metal-2DEG Hybrid Systems with Rashba Spin-Orbit Coupling, *Phys. Rev. Lett.* **88**, 029701 (2001).
- [51] The resonant peak slightly deviates from zero energy, because the Dirac-type potential does not have particle-hole symmetry, i.e., it has the same sign for both spin-up and spin-down states. Whether the peak is on the left or right side of zero energy depends on the sign of the barrier strength Z . Here, we have taken the bands in the normal metal with a positive effective mass, so that Z is positive. If we would have used the bands with negative mass, then the barrier Z for the holelike particle would have also been negative, and the corresponding peak would appear on the right side of the zero energy.
- [52] S. Datta, *Electronic Transport in Mesoscopic Systems* (Cambridge University Press, Cambridge, England, 1995).
- [53] D. A. Ryndyk, *Theory of Quantum Transport at Nanoscale: An Introduction* (Springer International, Cham, 2016).
- [54] S. Takahashi and S. Maekawa, Spin current in metals and superconductors, *J. Phys. Soc. Jpn.* **77**, 031009 (2008).
- [55] F. Mireles and G. Kirczenow, Ballistic spin-polarized transport and Rashba spin precession in semiconductor nanowires, *Phys. Rev. B* **64**, 024426 (2001).
- [56] R. M. Stroud, A. T. Hanbicki, Y. D. Park, G. Kioseoglou, A. G. Petukhov, B. T. Jonker, G. Itskos, and A. Petrou, Reduction of Spin Injection Efficiency by Interface Defect Spin Scattering in $\text{ZnMnSe}/\text{AlGaAs-GaAs}$ Spin-Polarized Light-Emitting Diodes, *Phys. Rev. Lett.* **89**, 166602 (2002).
- [57] I. Žutić, J. Fabian, and S. Das Sarma, Spintronics: Fundamentals and applications, *Rev. Mod. Phys.* **76**, 323 (2004).
- [58] T. Guan *et al.*, Evidence for Half-Metallicity in n -type HgCr_2Se_4 , *Phys. Rev. Lett.* **115**, 087002 (2015).